

# The physical and chemical structure of Sagittarius B2

## VII. UCH<sub>II</sub> regions in SgrB2

F. Meng<sup>1</sup>, Á. Sánchez-Monge<sup>1</sup>, P. Schilke<sup>1</sup>, A. Ginsburg<sup>2</sup>, A. Schmiedeke<sup>3</sup>, A. Schwörer<sup>1</sup>, C. DePree<sup>4</sup>, V. S. Veena<sup>1</sup>, and Th. Möller<sup>1</sup>

<sup>1</sup> I. Physikalisches Institut, Universität zu Köln, Zülpicher Str. 77, D-50937 Köln, Germany  
e-mail: meng@ph1.uni-koeln.de

<sup>2</sup> UFL, USA

<sup>3</sup> Max Planck Institute for Extraterrestrial Physics, Giessenbachstrasse 1, D-85748 Garching, Germany

<sup>4</sup> Agnes Scott College, 141 E. College Ave., Decatur, GA 30030, USA

Received ; accepted

### ABSTRACT

**Context.** The giant molecular cloud Sagittarius B2 (hereafter SgrB2) is the most massive region with ongoing high-mass star formation in the Galaxy. Dust cores and UC-H<sub>II</sub> regions are spread all over SgrB2. Giant dust and ionized bubbles fill the envelope of SgrB2.

**Aims.** We seek to characterize the association of UC-H<sub>II</sub> regions and the 270 dust cores.

**Methods.** We use the Very Large Array in its A, CnB and D configurations, and in the frequency bands C (4–8 GHz) and X (8–12 GHz) to observe the whole SgrB2 complex.

**Results.** Dust cores and UC-H<sub>II</sub> regions are spread all over SgrB2.

**Conclusions.** The envelope has star forming activities long ago. The star formation in SgrB2(M) and (N) is newer.

**Key words.** Stars: formation – Stars: massive – Radio continuum: ISM – Radio lines: ISM – ISM: clouds – ISM: individual objects: SgrB2

### 1. Introduction

The giant molecular cloud Sagittarius B2 (SgrB2) is the most massive ( $\sim 10^7 M_{\odot}$ ) region with ongoing high-mass star formation in the Galaxy. SgrB2 has a higher density ( $> 10^5 \text{ cm}^{-3}$ ) and dust temperature ( $\sim 50\text{--}70 \text{ K}$ ) compared to other star forming regions in the Galactic plane. Additionally, SgrB2 is located at a projected distance of only  $\sim 100 \text{ pc}$  to the Galactic center. These features make SgrB2 an excellent case to study high-mass star formation in an extreme, high-pressure environment. Such an environment resembles nearby starburst galaxies. Understanding the structure of the SgrB2 molecular cloud complex is necessary to comprehend the most massive star forming region in our Galaxy, which at the same time provides an unique opportunity to study in detail the nearest counterpart of the extreme environments that dominate star formation in the Universe.

In the central  $\sim 2 \text{ pc}$  of SgrB2, there are the two well-known and studied hot cores SgrB2(N) and SgrB2(M) (see e.g., Schmiedeke et al. 2016; Sánchez-Monge et al. 2017), which contain at least 70 high-mass stars with spectral types from O5 to B0 (see e.g., Gaume et al. 1995; De Pree et al. 1998, 2014). Surrounding the two hot cores, there is a larger envelope (hereafter *the envelope*) with a radius of 20 pc that contains more than 99% of the total mass of SgrB2 (Schmiedeke et al. 2016). The envelope has lower density  $n_{\text{H}} = 10^3 \text{ cm}^{-3}$  and lower gas temperature  $T \sim 50 \text{ K}$  compared to the two central hot cores of SgrB2. Alongside with the active high-mass star forming activities discovered in SgrB2(N) and SgrB2(M), hints of star formation happening in the envelope are also revealed. Ginsburg

et al. (2018), with ALMA at 3 mm, revealed more than 271 high-mass protostellar cores distributed throughout the entire SgrB2, including the envelope. The luminosities of these dust cores suggest that they must contain objects with stellar masses larger than  $8 M_{\odot}$ . Due to the high extinction in infrared bands towards SgrB2 (see Meng et al. 2019), direct evidence of the existence of high-mass stars embedded in these cores are missing. However, since that high-mass stars ionize the neutral material surrounding them, the presence and properties of the associated H<sub>II</sub> regions reflect the evolutionary stages of these dust cores (see e.g. González-Avilés et al. 2005; Breen et al. 2010). Additionally, since that the free-free emission from H<sub>II</sub> regions may extend from cm to mm wavelength in spectral domain (see e.g. Sánchez-Monge et al. 2013), measuring the luminosities of the associated H<sub>II</sub> regions can help us better constrain the luminosities of the dust cores. Therefore, to further characterize the evolutionary stages and physical properties of these dust cores, we aim to investigate the possible H<sub>II</sub> regions associated with them.

The H<sub>II</sub> regions in SgrB2 were targeted by various previous studies. (Mehringer et al. 1993) observed the entire SgrB2 with VLA in 20, 6, and 3.6 cm bands and identified 15 H<sub>II</sub> regions. The resolutions range from  $\sim 20''$  to  $\sim 3''$  from 20 to 3.6 cm, which correspond to 0.8–0.12 pc. The 15 H<sub>II</sub> regions, except two unresolved ones, all have size  $> 2''$ . Since that the 271 dust cores may contain high-mass stars newly formed (Ginsburg et al. 2018), the associated H<sub>II</sub> regions may be UCH<sub>II</sub> and HCH<sub>II</sub> regions, which typically have sizes from  $\sim 0.01 \text{ pc}$  to  $\sim 0.1 \text{ pc}$  (see e.g. Kurtz 2002; González-Avilés et al. 2005; Kurtz 2005; Breen et al. 2010). Such a resolution is not sufficient to resolve the UCH<sub>II</sub>

and HCHII regions. Gaume & Claussen (1990); Gaume et al. (1995) observed SgrB2 at 7 mm and 1.3 cm and achieved resolutions of 0.065'' and 0.25'', respectively. These high-resolution observations focus only on Sgr B2(N) and Sgr B2(M), which do not cover the envelope that the dust cores that are distributed throughout, especially SgrB2(DS) (see e.g. Ginsburg et al. 2018; Meng et al. 2019) that ~80 of the cores reside. LaRosa et al. (2000); Law et al. (2008a,b) have also observed the entire SgrB2 in cm wavelength but with resolutions not high enough to study UCHII and HCHII regions.

In this paper, we present Very Large Array (VLA) observations of the entire SgrB2 in the frequency regime 4–8 GHz, with configurations A, BnC and D. Thus, this study reaches resolutions of  $\sim 0.05$ . For comparison, we also include analysis of the 3 mm image (Ginsburg et al. 2018) as well as the newly acquired SiO (5–4) data, both of which were observed with ALMA (the Atacama Large Millimeter/submillimeter Array). In Sect. 2 we describe the observations as well as the data reduction process. Sect. 3 shows the results. In Sect. 4 we discuss the results. Finally, we summarize this paper in Sect. 6.

## 2. Observations and data reduction

We used the VLA in its A, CnB, and D configurations to observe the entire SgrB2 complex in the frequency bands C (4–8 GHz) and X (8–12 GHz). The observations with the CnB and D configurations were described in (Meng et al. 2019). The observations with the A configuration were conducted from October 1 to 12, 2016 (project 16B-031, PI: F. Meng). For both bands, we used 64 spectral windows with a bandwidth of 128 MHz each. Mosaic mode was used, with 10 and 18 pointings for each band, respectively. The primary beam of each pointing is 7.5' and 4.5' respectively. Quasar 3C286 was used as the flux and bandpass calibrator, the SED of which is  $S_\nu = 5.059 \pm 0.021 \text{ Jy} \times (S/8.435 \text{ GHz})^{-0.46}$  from 0.5 to 50 GHz (Perley & Butler 2013). The quasar J1820-2528, the flux of which is 1.3 Jy in the C and X bands, was used as phase calibrator. The calibration was done using the standard VLA pipelines provided by the NRAO<sup>1</sup>.

Calibration and imaging were done in Common Astronomy Software Applications (CASA) 4.7.2 (McMullin et al. 2007). The details of data processing of data from CnB and D configurations are described in (Meng et al. 2019), which results in two images in C and X band, respectively. The A configuration data were originally taken every 2 s. To shorten the time of processing, we applied `timebin` in CASA to the measurement sets, which averaged the data taken within 10 s into one data point. All the pointings of the mosaic in each band were primary beam corrected and the mosaic was imaged using the CASA task `tclean`. With a robust factor of 0, the images of the C and X bands have synthesized beams of  $0.62'' \times 0.28''$ , with a position angle (PA) of  $7.27^\circ$  and  $0.36'' \times 0.15''$  (PA =  $3.12^\circ$ ), respectively. The PA is defined positive north to east. To suppress the spatial filtering effect of the A configuration image, we applied the `feather` algorithm to combine the images from A configuration and the images from CnB and D configuration. The combined images have resolutions identical to that of A configuration images, while are sensitive to spatial scales up to  $\sim 240''$  and  $\sim 145''$  in C and X Band, respectively. The sensitivities of the observations are described in Sect. 3.

<sup>1</sup> The National Radio Astronomy Observatory is a facility of the National Science Foundation operated under cooperative agreement by Associated Universities, Inc.

Ancillary data include the 3 mm continuum and SiO (5–4) data. The 3 mm continuum data covers frequency range from 89.5 to 103.3 GHz. The image in 3 mm has a resolution of  $0.54'' \times 0.46''$  (PA =  $68.31^\circ$ ). The observational details of the 3 mm data are described by Ginsburg et al. (2018). The SiO (5–4) emission was observed with ALMA (Project 18A-229, P.I. A. Ginsburg). For the details of the observation and data reduction, see Ginsburg et al. (in prep.). The resolution is  $0.35'' \times 0.24''$ , with P.A. of  $-80^\circ$ . The spectral resolution is  $1.35 \text{ km s}^{-1}$ . The typical RMS of the image is 0.9 mJy/beam. The observation covers SgrB2(S) and the eastern part of SgrB2(DS).

## 3. Results

In this section, we present the image of SgrB2 in 6 cm and the UCHII regions identified in it. We also compared between these ionized cores with dust cores identified in 96 GHz. Statistics of the properties of these UCHII regions are shown.

We show the images in C and X bands in Fig. 1, in which the known regions ‘N’, ‘M’, ‘S’, ‘AA’, ‘DS’, and ‘V’ are denoted. The nomenclature of these regions follows Mehringer et al. (1992, 1993); Ginsburg et al. (2018); Meng et al. (2019). Although that deep CLEAN and self calibration were preformed in data processing, the high dynamic range of the images ( $\sim 10^3$ ) hinders the elimination of artifacts. As shown in Fig. 1, the C band image displays multi-scale prominent signal all over SgrB2, while the X band image is highly contaminated by the artifacts that from which the real emission is hard to distinguished. Therefore, we do not take the X band image into account in the following analysis. The C band image is called ‘6 cm image’ in the following analysis. Due to the non-homogeneity of the artifacts over the map, we do not give an RMS (root-mean-square) value to represent the noise value of the 6 cm image, but evaluate the spatial varying RMS. The procedures of generation the RMS maps are described in Sect. A. As shown in Fig. A.1, the RMS of the 6 cm image varies from  $\sim 0.02$  mJy/beam to  $\sim 0.2$  mJy/beam. The RMS of the 3 mm map, as shown in Fig. A.2, ranges from  $\sim 0.1$  mJy/beam to  $\sim 0.4$  mJy/beam.

## References

- Breen, S. L., Ellingsen, S. P., Caswell, J. L., & Lewis, B. E. 2010, MNRAS, 401, 2219
- De Pree, C. G., Goss, W. M., & Gaume, R. A. 1998, ApJ, 500, 847
- De Pree, C. G., Peters, T., Mac Low, M. M., et al. 2014, ApJ, 781, L36
- Gaume, R. A. & Claussen, M. J. 1990, ApJ, 351, 538
- Gaume, R. A., Claussen, M. J., de Pree, C. G., Goss, W. M., & Mehringer, D. M. 1995, ApJ, 449, 663
- Ginsburg, A., Bally, J., Barnes, A., et al. 2018, ApJ, 853, 171
- González-Avilés, M., Lizano, S., & Raga, A. C. 2005, ApJ, 621, 359
- Kurtz, S. 2002, in Astronomical Society of the Pacific Conference Series, Vol. 267, Hot Star Workshop III: The Earliest Phases of Massive Star Birth, ed. P. Crowther, 81
- Kurtz, S. 2005, in IAU Symposium, Vol. 227, Massive Star Birth: A Crossroads of Astrophysics, ed. R. Cesaroni, M. Felli, E. Churchwell, & M. Walmsley, 111–119
- LaRosa, T. N., Kassim, N. E., Lazio, T. J. W., & Hyman, S. D. 2000, AJ, 119, 207
- Law, C. J., Yusef-Zadeh, F., & Cotton, W. D. 2008a, ApJS, 177, 515
- Law, C. J., Yusef-Zadeh, F., Cotton, W. D., & Maddalena, R. J. 2008b, ApJS, 177, 255
- McMullin, J. P., Waters, B., Schiebel, D., Young, W., & Golap, K. 2007, in Astronomical Society of the Pacific Conference Series, Vol. 376, Astronomical Data Analysis Software and Systems XVI, ed. R. A. Shaw, F. Hill, & D. J. Bell, 127
- Mehringer, D. M., Palmer, P., Goss, W. M., & Yusef-Zadeh, F. 1993, ApJ, 412, 684
- Mehringer, D. M., Yusef-Zadeh, F., Palmer, P., & Goss, W. M. 1992, ApJ, 401, 168

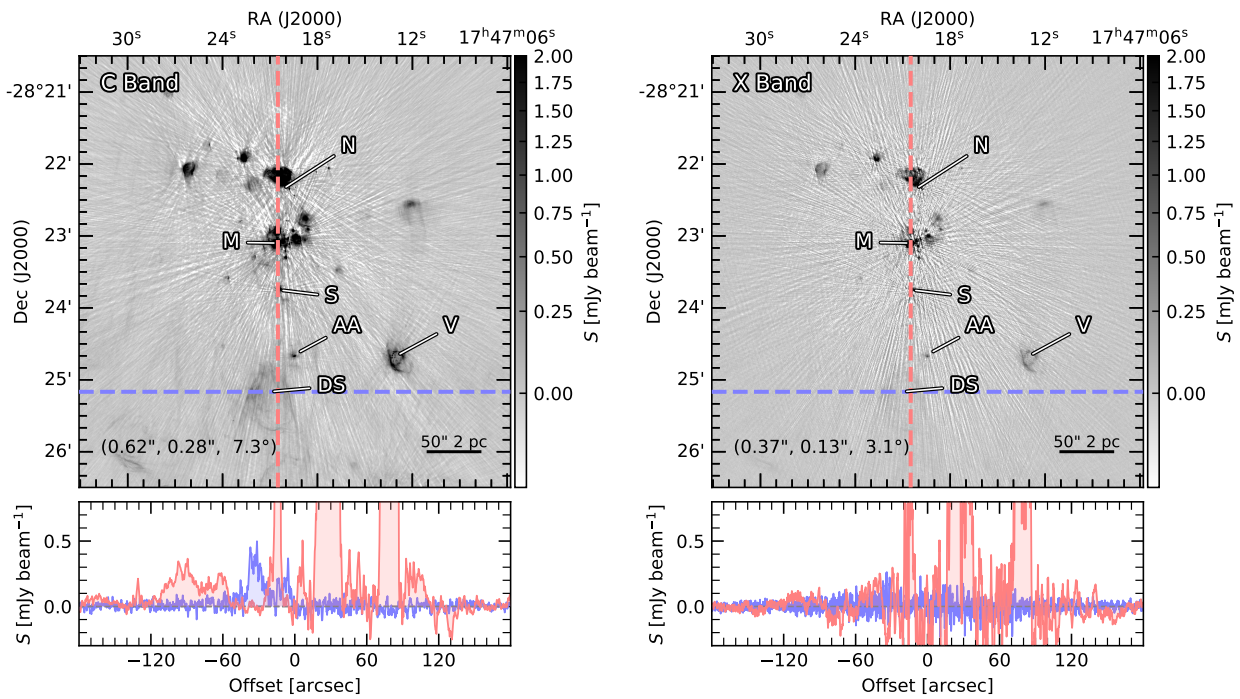


**Fig. 1.** Images in C and X Bands. Notable regions are marked. Beam sizes are marked on the lower left corner of each panel, in format ( $\theta_{\text{maj}}$ ,  $\theta_{\text{min}}$ , PA). Each image has two profile cuts, in blue and red. The offset of each profile increase from left to right and from bottom to top. The profiles are below each image.

Meng, F., Sánchez-Monge, Á., Schilke, P., et al. 2019, A&A, 630, A73  
 Perley, R. A. & Butler, B. J. 2013, ApJS, 204, 19  
 Sánchez-Monge, Á., Kurtz, S., Palau, A., et al. 2013, ApJ, 766, 114  
 Sánchez-Monge, Á., Schilke, P., Schmiedeke, A., et al. 2017, A&A, 604, A6  
 Schmiedeke, A., Schilke, P., Möller, T., et al. 2016, A&A, 588, A143  
 Virtanen, P., Gommers, R., Oliphant, T. E., et al. 2020, Nature Methods, 17, 261

## Appendix A: RMS maps

In this section we introduce the production of the RMS maps of the 6 cm and 3 mm data used in this paper. Firstly, we masked out the image at where the signal is above a certain threshold to create a ‘masked image’. In this paper, the threshold for both of 6 cm and 3 mm images were 1 mJy/beam. In SciPy (Virtanen et al. 2020), we applied the algorithm `ndimage.generic_filter`, to the masked image. The filter function was defined as a standard deviation function. A parameter called `size` controls the subregion of the masked image that is given as input to the filter algorithm each time. For both of 6 cm and 3 mm images, `size` was set to 100 pixels, which corresponds to 5''. Thus, an masked RMS map was generated, in which where the signal was above the threshold is empty. To fill the masked regions, we used cubic interpolation over the whole image. In the interpolation, patches of the size of  $100 \times 100$  pixels ( $5'' \times 5''$ ) were treated as one data point, which reduces the complexity of the computation. Thus we obtain rms maps as shown in Fig. A.1 and A.2

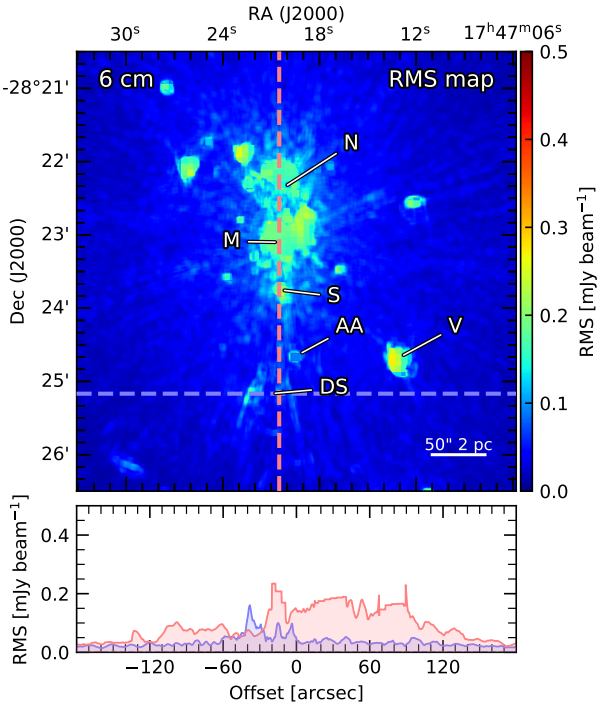


**Fig. A.1.** RMS map of 6 cm image. The image has two profile cuts, in blue and red. The offset of each profile increase from left to right and from bottom to top. The profile is below each image.

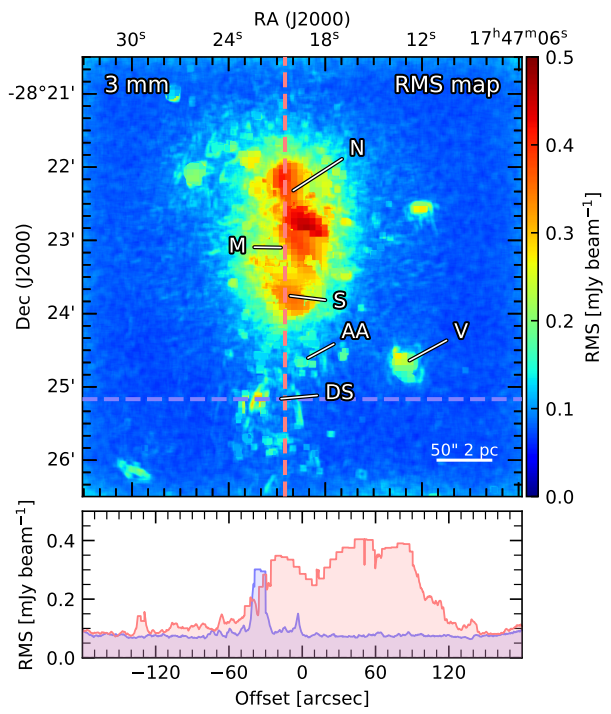


**Fig. A.2.** RMS map of 3 mm image. The image has two profile cuts, in blue and red. The offset of each profile increase from left to right and from bottom to top. The profile is below each image.